Sensitivity analysis of fuel production by carbon monoxide electrolysis

Dominik Hulak[a], Leszek Remiorz[a]

[a] *Silesian University of Technology, Gliwice, Poland, email: dominik.hulak@polsl.pl* ***(CA)***

Abstract:

The electrochemical reduction of carbon monoxide and carbon dioxide to value-added products is a promising technology for production of sustainable fuels, CO_2 capture and electrification. Electrolysis systems are often studied using mathematical modelling. A reliable and validated model allows for the observation of parameters that are difficult to measure and for the examination of the system in many operating states, while minimising the number of costly prototypes and improving the design process. One of the key stages in verifying the correctness of the model is sensitivity analysis. A properly performed sensitivity analysis allows, among other things, to determine which measurements should be performed with the highest accuracy, how the type of material affects the operation of the device, and which component dimensions are most critical. In this work, we therefore present a comprehensive sensitivity analysis of a carbon monoxide electrolysis system aimed at the production of fuels, such as n-propanol, ethylene and ethanol. Based on an original process model, we investigate the influence of key parameters, including temperature, reaction kinetics and resistance, on reactor performance. Sensitivity was determined both locally (using one-at-a-time approach) and globally (using Sobol's method). Based on our analyses, we identify parameters that are crucial for process efficiency and provide practical guidance on measurements and design in electrolyser systems. The presented analysis provides insight into model robustness and parameter hierarchy, thereby supporting more reliable system optimisation and scale-up.

Keywords:

Electrolysis; Carbon monoxide; Electrochemical reduction; Modelling; Sensitivity analysis.

1. Introduction

Carbon dioxide electrolysis (CO_2E) stands as one of the most promising technologies for fuel and energy carrier production. When powered using renewable electricity and captured CO_2, it enables the synthesis of sustainable methane, ethanol, ethylene, and n-propanol, among others [1,2]. Their formation is favoured in highly alkaline electrolytes, which are susceptible to carbonate formation [3]. This limits the maximum single-pass CO_2 conversion rate, lowers its availability in the catalyst, may require energy intensive electrolyte regeneration, and could lead to salt precipitation [3–5]. One of the investigated solutions is tandem electrolysis, where CO_2 is first reduced to CO in a carbonate-free system (e.g. in acidic conditions or solid-oxide cell), and then CO is further reduced to target product [6–8].

Due to the shared reaction pathway, the same products can be obtained by CO electrolysis (COE), and different copper-based catalysts show high performance [9,10]. To investigate COE and CO_2E, numerous mathematical modelling frameworks have been developed [11–15]. These most often rely on computationally-demanding multi-physics simulations. However, in techno-economic assessments or sensitivity analyses of energy systems, simplified models often provide sufficient accuracy, while being easier to implement. Models of this kind have been used in water electrolysis [16,17] or CO_2 electrolysis in solid-oxide cells [18].

To investigate the process of carbon monoxide electrolysis and aid the design of future devices, we describe a simplified process modelling framework. Upon validation, we perform an extensive sensitivity analysis of the model. This will enable the identification of which parameters have the greatest impact on the cell performance, and therefore which should be prioritised in experimental studies. In addition, we present an analysis of parameters whose impact is difficult or impractical to determine through measurements.

2. Electrolysis modelling

2.1. Electrochemical model

The model of electrochemical CO reduction is based on [19]. The main equation describing the cell voltage U_{cell} is

$$U_{cell} = U_{rev} + U_{act,c} + U_{act,a} + U_{ohm}, \quad (1)$$

where U_{rev} is the reversible voltage, U_{ohm} is the ohmic voltage drop, while $U_{act,c}$ and $U_{act,a}$ are cathodic and anodic activation overpotentials, respectively. The reversible potential of the cell is the difference between anodic $E_{rev,a}$ and cathodic $E_{rev,c}$ reversible potentials. Given a conventional OER-based anode, $E_{rev,a}$ is equal to 1.23 V vs. RHE, while $E_{rev,c}$ depends on the selected reference cathodic reaction. For n-propanol $E_{rev,c}$ is 0.20 V vs RHE, and hence reversible voltage is 1.03 V. These values are true under standard conditions, that is temperature $T = 298.15$ K, pressure $p = 1$ bar and solute concentrations $C = 1$ mol/dm^3. To account for non-standard conditions, Nernst equation is used

$$E_{rev} = E^0_{rev} - \frac{R_{gas}T}{zF} \ln Q \quad (2)$$

where E^0_{rev} is the standard reversible potential, $R_{gas} = 8.314$ J/mol/K is the universal gas constant, z is the amount of electrons transferred, $F = 96485$ C/mol is the Faraday's constant, and Q is the reaction quotient. The value of Q is here approximated by the ratio of product and substrate concentrations.

The anodic and cathodic overpotentials, which are defined as the difference between reversible potential and the applied E_{appl} potential, determine the partial current densities i. Here they are described by a modified version of a concentration-dependent Tafel equation

$$i = \left(i_0 \exp\frac{\alpha F U_{act}}{RT}\right)\left(\frac{c^{\mathrm{CO}}}{c^{\mathrm{CO}}_{ref}}\right)^{\gamma}\left(\frac{1}{1+\exp[\beta_1(U_{act}+\beta_2)]}\right) \quad (3)$$

The first term of Eq. (3) is the standard formulation of Tafel expression, which describes the intensity of reaction under kinetic parameters i_0 and α. The second term is the concentration-dependence term, which takes into account the decrease of substrate concentration in the catalyst zone. The sensitivity towards CO concentration depends on the reaction order γ, which is assumed to be equal to 1 for all considered reactions. The last term is here introduced to take into account the competition between cathodic reduction pathways. For cathodic hydrogen evolution reaction, the CO concentrations are replaced by water activity, and by OH- activity for the anodic oxygen evolution reaction.

The kinetic parameters i_0 and α are described by

$$i_0 = 10^{-(\eta_{10}-b)/b} \quad [\mathrm{mA/cm^2}], \quad (4)$$

$$\alpha = \frac{2303RT}{bF} \quad [\text{dimensionless}], \quad (5)$$

where Tafel slope b is expressed in mV/dec, onset potential η_{10} in mV, R_{gas} in J/mol/K, T in K and F in C/mol. The parameters b, η_{10}, β_1 and β_2 are fit to experimental data separately for each product, and are obtained at temperature T. For $T' \neq T$, the value of i_0 can be adjusted using equation

$$i_0(T') = i_0(T) \exp\left[-\frac{E_a}{R_{gas}}\left(\frac{1}{T'} - \frac{1}{T}\right)\right], \quad (6)$$

where E_a is the activation energy.

The ohmic losses can be calculated by Ohm's law as

$$U_{ohm} = IR_{cell} = i_{cell}AR_{cell}, \quad (7)$$

where I is total current, $i_{cell} = \sum i_c = i_a$ is total cell current density, A is cell cross-section area and R_{cell} is cell resistance. In this model it is assumed that R_{cell} is a sum of resistances R of cell elements. These include bipolar plate $R_{bp} = R_{bp,b} + R_{bp,ch}$ (base and channel), cathode $R_c = R_{c,\mathrm{GDL}} + R_{c,\mathrm{MPL}} + R_{c,\mathrm{CL}}$ (gas-diffusion layer GDL, microporous layer MPL and catalyst layer CL), catholyte R_{cat}, membrane R_{mem}, anolyte R_{ano} and anode resistance R_a, as well as contact resistance R_{cont} between certain elements. All values of R, with the exception of $R_{bp,ch}$ and R_{ano}, can be calculated as

$$R = \lambda\frac{\sigma}{A} = \frac{\sigma}{\kappa A} = \frac{\mathrm{ASR}}{A}, \quad (8)$$

where σ is the element's thickness, λ is the resistivity, κ is the conductivity, and ASR is the area-specific resistance. The values of λ, κ or ASR for the respective elements are listed in Table 1. As for $R_{bp,ch}$, due to its serpentine channel layout, the resistance is calculated as [20]

$$R_{bp,ch} = \frac{\lambda_{bp}\sigma_{ch}(2n_{bp}+1)}{2A(n_{bp}+1)}, \quad (9)$$

where n_{bp} is the number of flow channels. It is assumed that the bipolar plate is a square with a side length of $\sqrt{A}$, and that the width of each channel is equal to the width of each channel support. Due to the porosity of the anode, the resistance R_{ano} of the in-pore anolyte is determined as [21]

$$R_{ano} = \frac{\xi_a\sigma_a}{\varepsilon_a\kappa^{\mathrm{MOH}}_{ano}A}, \quad (10)$$

where ξ_a is the anode's tortuosity, ε_a is its porosity, and $\kappa^{\mathrm{MOH}}_{ano}$ is the conductivity of the anolyte. Furthermore, when calculating the resistance of the porous anode, the effective resistivity $\lambda_{eff,a}$ defined as

$$\lambda_{eff,a} = \frac{\lambda_a}{(1-\varepsilon_a)^{3/2}}, \quad (11)$$

where λ_a is the resistivity of non-porous anode material, is used in Eq. (8). Lastly, the considered R_{cont} are flow-field/cathode and membrane/anode resistance, as well as interlayer resistance between cathode layers (GDL/MPL and MPL/CL).

2.2. Mass balance and transport model

To evaluate the values of E_{rev} per Eq. (2) and i per Eq. (3), species concentrations in the catalyst areas need to be established. The starting point for this is the mass balance for all substances present in the system. The three balancing domains are the flow-field plate, the catholyte, and the anolyte. For each of them

$$\dot{n}_{in} + \dot{n}_{gen} = \dot{n}_{out} + \dot{n}_{cons}, \quad (12)$$

where $\dot{n}_{in}$ is the inlet molar flux, $\dot{n}_{out}$ is the outlet molar flux, $\dot{n}_{gen}$ is the generated flux and $\dot{n}_{cons}$ is the consumed flux.

The only substance at the inlet of flow-field is CO with a volumetric flux of $\dot{V}_{in,FF}^{\mathrm{CO}}$. Under the ideal gas assumption, the molar flux $\dot{n}_{in,FF}^{\mathrm{CO}}$ is calculated via

$$\dot{n} = \frac{\dot{V}\, p}{R_{gas} T}, \quad (13)$$

where p is gas pressure. Part of the CO ($\dot{n}_{cons,ff}^{CO}$) diffuses into the reaction area where it is consumed, while the remaining part $\dot{n}_{out,FF}^{\mathrm{CO}} = \dot{n}_{in,FF}^{\mathrm{CO}} - \dot{n}_{cons,FF}^{CO}$ goes to the outlet. The amount of consumed CO is proportional to the generated fluxes of all reduction products, as per

$$\dot{n}_{cons} = \sum_{prod} k\, \dot{n}_{gen}^{prod}, \quad (14)$$

where k is the stochiometric index indicating the number of moles of CO consumed per mole of product (e.g. $k = 3$ for n-propanol and $k = 0$ for hydrogen). The values of $\dot{n}_{gen}^{prod}$ are calculated as

$$\dot{n}_{gen}^{prod} = \frac{iA}{zF}. \quad (15)$$

The products considered in the flow-field domain are the gas products, i.e. methane, ethylene and hydrogen, and their generated fluxes are equal to the outlet fluxes. The outlet volumetric flux is calculated by Eq. (14) for $\dot{n}_{out,FF} = \dot{n}_{out,FF}^{\mathrm{CO}} + \dot{n}_{out,FF}^{\mathrm{H_2}} + \dot{n}_{out,FF}^{\mathrm{CH_4}} + \dot{n}_{out,FF}^{\mathrm{C_2H_4}}$.

When it comes to the catholyte balance, a volumetric flux $\dot{V}_{in,cat}$ of aqueous electrolyte solution with a concentration of C_{cat}^{MOH} is defined at the inlet. The electrolyte inlet flux $\dot{n}_{in,cat}^{\mathrm{MOH}}$ is calculated as

$$\dot{n}_{in,cat}^{\mathrm{MOH}} = \dot{V}_{in,cat} C_{cat}^{\mathrm{MOH}}, \quad (16)$$

and the water inlet flux $\dot{n}_{in,cat}^{\mathrm{H_2O}}$ is calculated from the balance of binary solution as

$$\dot{n}_{in,cat}^{\mathrm{H_2O}} = \dot{V}_{in,cat} \frac{\rho_{in,cat} - C_{cat}^{\mathrm{MOH}} M^{\mathrm{MOH}}}{M^{\mathrm{H_2O}}}, \quad (17)$$

where $\rho_{in,cat}$ is the inlet solution density and M is the molar mass. Similarly to CO, part of the water entering the catholyte boundary is consumed ($\dot{n}_{cons}^{\mathrm{H_2O}}$), and the remaining part goes to the outlet ($\dot{n}_{out}^{\mathrm{H_2O}}$). The value of $\dot{n}_{cons}^{\mathrm{H_2O}}$ is calculated by Eq. (15) for the appropriate values of k. The liquid products considered in the catholyte balance are acetic acid, ethanol, allyl alcohol and n-propanol. Their respective fluxes are calculated using Eq. (16) and are equal to outlet fluxes. The outlet volumetric flux, under the assumption that $\rho_{in,cat} = \rho_{out,cat}$, is calculated as

$$\dot{V}_{out,cat} = \frac{\sum \dot{n}_{out} M_{out}}{\rho_{out,cat}}. \quad (18)$$

The mass balance for the anolyte is calculated in the same way as for the catholyte. The main differences are that water is consumed in the reaction and that the only product is oxygen. Both are still calculated via Eqs. (15) and (16), respectively. Furthermore, the product oxygen is excluded from the outlet volumetric flux calculated by Eq. (19).

Knowing the molar and volumetric fluxes at all inlets and outlet, the species concentrations at these points can be determined as

$$C_{in/out} = \frac{\dot{n}_{in/out}}{\dot{V}_{in/out}}. \quad (19)$$

The inlet and outlet concentrations are used to calculate the bulk concentrations, which will be further used to calculate the concentrations in catalyst areas. The bulk CO concentration in the flow-field is calculated as

$$C_{bulk}^{\mathrm{CO}} = \frac{C_{in,FF}^{\mathrm{CO}} - C_{out,FF}^{\mathrm{CO}}}{\log \frac{C_{in,FF}^{\mathrm{CO}}}{C_{out,FF}^{\mathrm{CO}}}}, \quad (20)$$

while for the remaining substances and domains, it is $C_{bulk} = 0.5(C_{in} + C_{out})$. It is assumed that the bulk concentrations of OH^- ions are equal to the bulk concentrations of their respective electrolytes. Given the bulk concentrations of CO, H_2, CH_4 and C_2H_4, their concentrations at GDL/MPL interface can be calculated via Fick's diffusion law

$$\dot{n} = D\frac{\Delta C}{\sigma}A, \tag{21}$$

where D is the diffusion coefficient and $\dot{n}$ is either the consumption (for CO) or generation flux (for products). In that case, the thickness of the GDL layer σ_{GDL} must be used. Similarly, using Eq. (22), it is possible to determine the liquid product and OH^- ion concentrations at the cathode/catholyte interface ($C_{c,CL/cat}$) for a boundary layer thickness $\sigma_{BL,cat}$, as well as the OH^- ion concentrations at the anolyte/anode interface ($C_{ano/a,\mathrm{CL}}$) for a boundary layer thickness $\sigma_{BL,ano}$. Furthermore, knowing the values of $C_{GDL/MPL}$, Eq. (22) allows the determination of concentrations at the MPL/catalyst interface ($C_{MPL/c,\mathrm{CL}}$).

It was assumed that anodic reactions occur only on its surface. Therefore, the $C_{ano/a,\mathrm{CL}}$ values were used directly in determining Q and E_{rev}. However, cathodic reactions occur in a catalyst layer of thickness $\sigma_{c,\mathrm{CL}}$. A reaction-diffusion model [22] was used to describe the concentration profile in the layer

$$0 = D\frac{\mathrm{d}^2C}{d\sigma^2} \pm \frac{\dot{n}}{V}, \tag{22}$$

where $\dot{n}/V$ denotes the volumetric reaction term ("+" for generation, "-" consumption). For gaseous species V denotes the pore volume filled with gas V_{gas}, described by

$$V_{gas} = \varepsilon_{c,\mathrm{CL}}\sigma_{c,\mathrm{CL}}A\left[1 - \left(\frac{r_{c,\mathrm{CL}} - \sigma_{c,\mathrm{CL}}^{\mathrm{H_2O}}}{r_{c,\mathrm{CL}}}\right)^2\right], \tag{23}$$

where $r_{c,\mathrm{CL}}$ is the catalyst pore radius and $\sigma_{c,\mathrm{CL}}^{\mathrm{H_2O}}$ is the thickness of the water layer covering the pore walls. In turn, V_{liquid} denotes the pore volume filled with liquid, described by

$$V_{liquid} = \varepsilon_{c,\mathrm{CL}}\sigma_{c,\mathrm{CL}}A\left(\frac{r_{c,\mathrm{CL}} - \sigma_{c,\mathrm{CL}}^{\mathrm{H_2O}}}{r_{c,\mathrm{CL}}}\right)^2. \tag{24}$$

Assuming that $\dot{n}/V$ is constant across the layer thickness, the average concentrations of species in the layer are described by

$$\overline{C}_{c,\mathrm{CL}} = C \pm R\frac{\sigma_{c,\mathrm{CL}}^2}{3D}. \tag{25}$$

Here, $C = C_{MPL/c,\mathrm{CL}}$ for gaseous species, $C = C_{c,\mathrm{CL}/cat}$ for aqueous species, and the sign convention is the same as for Eq. (23). The aqueous $\overline{C}_{c,\mathrm{CL}}$ concentrations can be used directly in Q and E_{rev} determination. However, because the in-pore gasses are not in direct contact with the catalyst, further calculations are required. The gaseous concentrations are first converted to partial pressures via

$$\overline{p}_{c,\mathrm{CL}} = \overline{C}_{c,\mathrm{CL}}R_{gas}T. \tag{26}$$

Next, it is assumed that only CO is dissolved, while gaseous products form as bubbles on the pore surface. The bubble pressure for products is described by

$$\overline{p}_{bubble,c,\mathrm{CL}}^{prod} = \frac{\overline{p}_{c,\mathrm{CL}}^{prod}p_c}{\sum_{prod}\overline{p}_{c,\mathrm{CL}}^{prod}} \text{ for } prod = H_2, CH_4, C_2H_4. \tag{27}$$

To account for CO solubility in water and salting-out effect, the dissolved CO concentration $\overline{C}_{diss,c,\mathrm{CL}}^{\mathrm{CO}}$ is described as

$$\overline{C}_{diss,c,\mathrm{CL}}^{\mathrm{CO}} = H^{\mathrm{CO}}\overline{p}_{c,\mathrm{CL}}^{\mathrm{CO}}10^{-K_s}, \tag{28}$$

where H^{CO} is Henry's constant [23] and K_s is Sechenov's constant [24]. Bubble pressures calculated via Eq. (28) and dissolved CO concentration calculated via Eq. (29) can be used in Q and E_{rev} determination. The values of diffusion coefficients for gasses are calculated using the Chapman-Enskog theory [25] in porous medium, while for the aqueous species they are taken from the literature [22,26,27].

2.3. Sensitivity analysis

To analyse the proposed models' sensitivity to input parameters X_i, local S_{local} and global S_{global} sensitivity indices are used. For the local analysis, one-at-a-time approach is employed, following the equation

$$S_{local} = \left(\frac{f(X_i + \Delta X_i)}{f(X_i)} - 1\right) \cdot 100\%, \tag{29}$$

where $f(X_i)$ and $f(X_i + \Delta X_i)$ determine the value of selected output parameter at the point X_i and when changed by ΔX_i. The sensitivity defined in this way indicates by how much the value of the selected function

will change when one of the parameters changes by ΔX_i. The values of X_i for all 40 considered variables are collected in Table 1.

In the global analysis, the Sobol' method is used [28]. The method estimates the direct influence of variable X_i on function output via Sobol' first order indices S_i, described by

$$S_{i,global} = \frac{\mathrm{Var}_{X_i}\left(E_{X_{\sim i}}(Y|X_i)\right)}{\mathrm{Var}(Y)} = \frac{V_i}{\mathrm{Var}(Y)}, \tag{30}$$

where Y denotes the model outputs. The interaction between two variables X_i and X_j is described by second order indices S_{ij}, as described by

$$S_{ij,global} = \frac{\mathrm{Var}_{X_{ij}}\left(E_{X_{\sim ij}}(Y|X_i,X_j)\right)-V_i-V_j}{\mathrm{Var}(Y)}. \tag{31}$$

The global indices are calculated for all 40 variables, as well as all possible combinations for the variables. Their values are true within ranges collected in Table 1.

Table 1. *Model variable values and ranges for sensitivity analyses.*

Num.	Parameter, unit	Value	Range	Source	Num.	Parameter, unit	Value	Range	Source
1	$E_{appl,c}$, V vs. RHE	-1.41	-1.3;-1.47	[10]	21	n_{bp}, -	33	10; 50	[10]
2	T, °C	25	20; 80	[10]	22	$\sigma_{c,\mathrm{CL}}^{\mathrm{H_2O}}$, nm	25	0.5; 100	A
3	p_c, bar	1	1; 5	A	23	$r_{c,\mathrm{MPL}}$, nm	50	10; 200	A
4	p_a, bar	1	1; 5	A	24	$r_{c,\mathrm{CL}}$, nm	50	10; 200	A
5	$\dot{V}_{in,\mathrm{FF}}^{\mathrm{CO}}$, cm³/min	1	1; 100	[10]	25	$\varepsilon_{c,\mathrm{GDL}}$, -	0.5	0.2; 0.8	A
6	$\dot{V}_{in,cat}$, cm³/min	0.15	0.1;0.2	[10]	26	$\varepsilon_{c,\mathrm{MPL}}$, -	0.5	0.2; 0.8	A
7	$\dot{V}_{in,ano}$, cm³/min	0.15	0.1;0.2	[10]	27	$\varepsilon_{c,\mathrm{CL}}$, -	0.5	0.2; 0.8	A
8	C_{cat}^{MOH}, mol/dm³	1	0.2; 2	[10]	28	ε_a, -	0.5	0.2; 0.8	A
9	C_{ano}^{MOH}, mol/dm³	1	0.2; 2	[10]	29	$\xi_{c,\mathrm{GDL}}$, -	2	1; 3	A
10	A, cm2	1	1; 15	[10]	30	$\xi_{c,\mathrm{MPL}}$, -	2	1; 3	A
11	$\sigma_{bp,b}$, mm	1	0.1; 5	A	31	$\xi_{c,\mathrm{CL}}$, -	2	1; 3	A
12	$\sigma_{bp,ch}$, µm	90	10; 500	[10]	32	ξ_a, -	2	1; 3	A
13	$\sigma_{c,\mathrm{GDL}}$, µm	205	50; 1000	[29]	33	$\mathrm{ASR}_{\mathrm{GDL}}$, mΩcm²	10	5; 15	[29]
14	$\sigma_{c,\mathrm{MPL}}$, µm	10	1; 100	[10]	34	κ_{MPL}, S/m	30	1; 100	[30]
15	$\sigma_{c,\mathrm{CL}}$, µm	2	0.1; 5	[10]	35	$\kappa_{c,\mathrm{CL}}$, S/m	15	1; 100	[30]
16	$\sigma_{BL,cat}$, µm	100	50; 200	A	36	κ_{mem}, S/m	10	0.1; 100	[31]
17	σ_{cat}, mm	1.5	0.1; 5	[10]	37	$\mathrm{ASR}_{\mathrm{FF}/c,\mathrm{GDL}}$, mΩcm²	8	1; 20	[30]
18	σ_{mem}, µm	60	10; 200	[10]	38	$\mathrm{ASR}_{c,\mathrm{GDL}/c,\mathrm{MPL}}$, mΩcm²	2	1; 20	[30]
19	$\sigma_{BL,ano}$, µm	10	1; 100	A	39	$\mathrm{ASR}_{c,\mathrm{MPL}/c,\mathrm{CL}}$, mΩcm²	3	1; 20	[30]
20	σ_a, mm	1.6	0.5; 3	[10]	40	$\mathrm{ASR}_{mem/a}$, mΩcm²	8	1; 20	A

A – assumption.

3. Results

To verify the model's assumptions, a validation was carried out based on experimental data from the literature presented in [10]. These data were selected because they include both the cathode half-cell potentials and the total cell voltages, which allows for a more extensive verification. In addition, most of the relevant parameters relating to the streams and cell geometry have been provided. The key validation parameters are summarised in the Table 1. The missing parameters were either assumed or taken from other sources in the literature. The anode kinetics of $\eta_{10} = 177$ mV and $b = 51.9$ mV/dec for NiFe catalyst was obtained from [32].

The validation is shown in Figure 1, and the fitted cathode kinetic parameters are summarised in Table 2. A comparison of the model and experimental data reveals a high degree of agreement in the voltage-current characteristics (Figure 2a), particularly in the range of low and moderate current densities. In this range, the fitting error is less than 50 mV. The largest error is observed at the measurement point with the highest current density. This may be due to an overestimated cell resistance and an underestimated activation overpotential. However, even this error does not exceed 100 mV, and so the overall fit can be considered satisfactory.

The good overall current agreement results from the good match in the partial current densities of the individual major (Figure 2b) and minor (Figure 2c) products. The current densities for $C_{1\text{-}2}$ products and hydrogen increase exponentially as the potentials become more negative, but taper off near -0.65 V vs RHE. This is most likely due to mass-transport limitations. This decline is not observable for methane, due to its very low fitted Tafel slope value. In the case of C3 products, a decrease in i was observed before the diffusion-limited regime. It is therefore reasonable to suspect that a change in the reaction pathway has occurred. Since Eq. (3) was applied, the decline could be described using parameters β_1 and β_2. For the other products, it was assumed that $\beta_1 \to \infty$ and $\beta_2 \to -\infty$, and therefore Eq. (3) was reduced to the more conventional concentration-dependent Tafel equation. The poorest fit was obtained for hydrogen. This may be due to greater competition between H_2O and CO for catalytic sites in a moderate potential range.

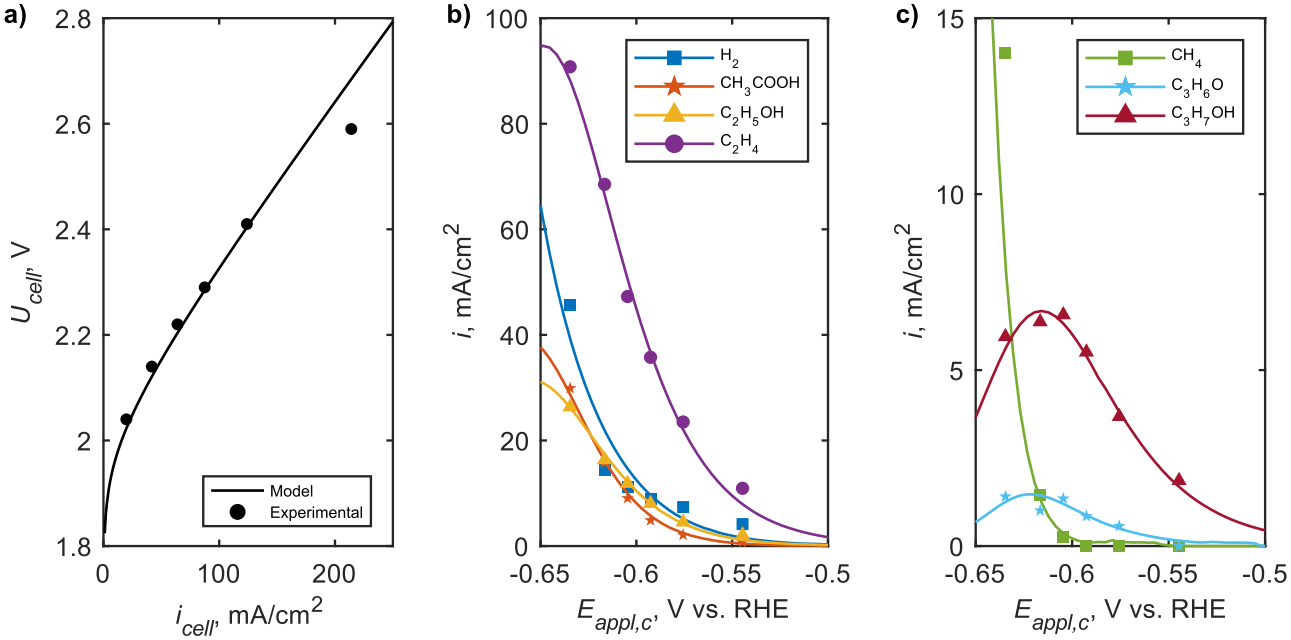

Figure 1. *Validation of the model's assumptions: (a) voltage-current characteristics, (b) major product distribution, (c) minor product distribution.*

Table 2*. Cathode fit kinetics.*

Product	b, mV/dec	η_{10}, mV	β_1, 1/mV	β_2, mV
H_2	55	602	$\to \infty$	$\to -\infty$
CH_3COOH	25	860	$\to \infty$	$\to -\infty$
CH_4	10	884	$\to \infty$	$\to -\infty$
C_2H_4	65	757	$\to \infty$	$\to -\infty$
C_2H_5OH	45	762	$\to \infty$	$\to -\infty$
C_3H_6O	50	770	0.1	-0.75
C_3H_7OH	70	790	0.06	-0.807

Based on a validated process model, a sensitivity analysis can be performed. The results of the local sensitivity analysis with respect to cell voltage $\boldsymbol{U_{cell}}$ are shown in Figure 2. They were obtained for the operating point defined by the parameters listed in Table 1 (excluding $\boldsymbol{E_{appl,c}}$) and $\boldsymbol{E_{appl,c}}$ of -0.584, -0.606 and -0.622 V vs. RHE (which correspond to current densities of 50, 100 and 150 mA/cm^2 at baseline, respectively). The value of each parameter was changed by $\boldsymbol{\Delta X} = 5\%$. The cathode kinetics remained unchanged and the parameters from Table 2 were used.

The local sensitivity analysis shows that the parameter with by far the highest sensitivity (regarding U_{cell}) is cathodic potential. A 5% change in its value results in a 34.6% increase in U_{cell} at -0.584 V vs RHE., a 43.8% increase at -0.606 V vs. RHE., and a 56.5% increase at -0.622 V vs. RHE. The second parameter, regardless of $E_{appl,c}$, is temperature, a change in which causes a U_{cell} increase of up to 5.8%. The other parameters have a lesser effect. A change in U_{cell} ranging from 0.1% to 1% was caused by 6 parameters at least negative potential, 8 at medium potential and 9 at the most negative potential. Two parameters, notably anodic pressure and volumetric anolyte flow have no impact on U_{cell}.

When comparing Figures 2a, 2b and 2c, it can be seen that the hierarchy of parameter sensitivity changes with potential (and thus also with current density). The variables whose influence increases as the potentials

become more negative are, in particular, the anolyte concentration and the parameters of the gas diffusion layer ($\xi_{c,\mathrm{GDL}}, \sigma_{c,\mathrm{GDL}}, \epsilon_{C,\mathrm{GDL}}$), whilst it decreases for the contact resistance parameters.

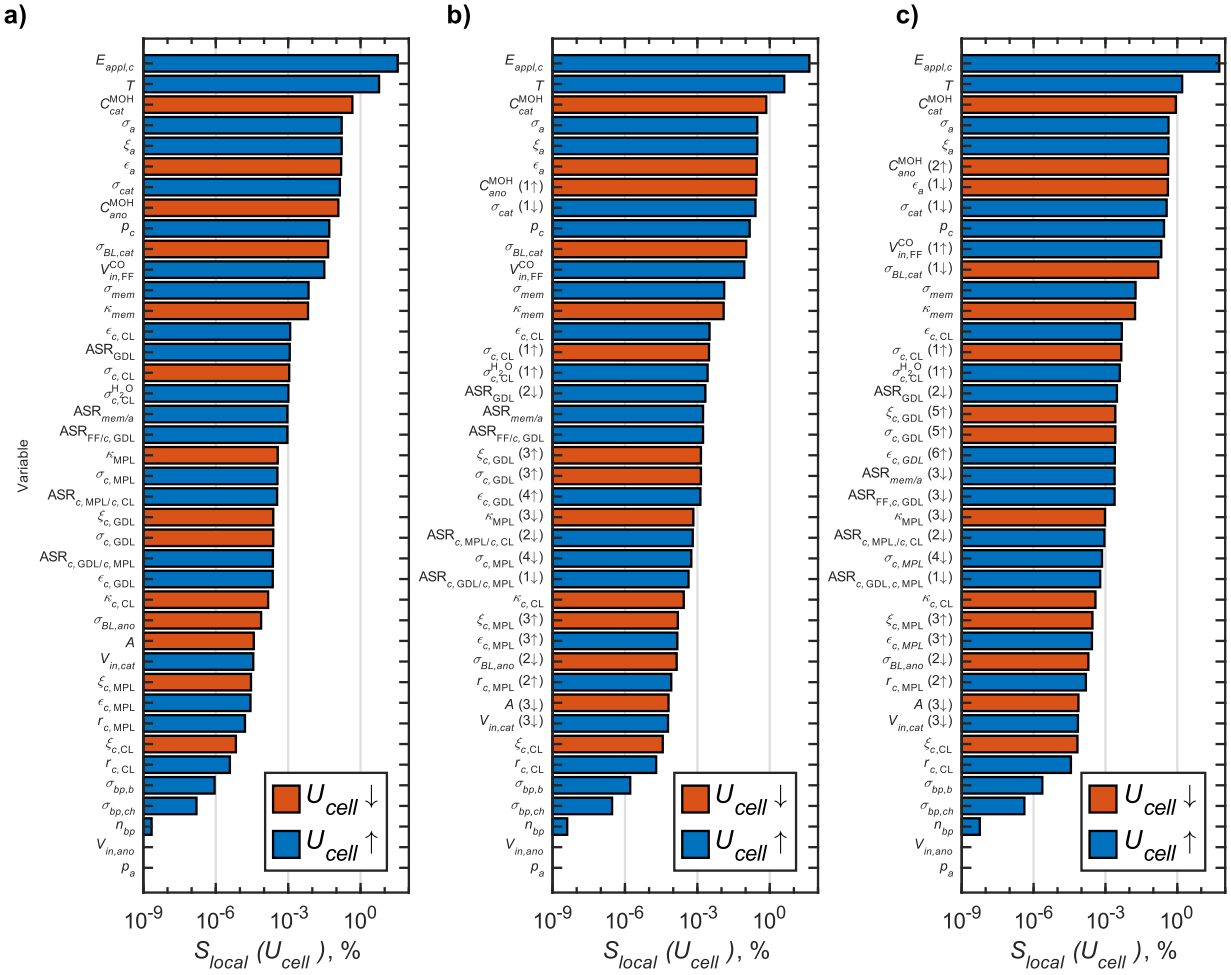

***Figure 2**. Local sensitivity analysis with respect to U_{cell}: values of S_{local} for $\Delta X = 5\%$ at (a) -0.584, (b) -0.606 and (c) -0.622 V vs. RHE for main model parameters.*

The analysis shown in Figure 2 does not include catalyst parameters. Therefore, their effect on the total current density i_{cell} is shown in Figure 3 for the same cathodic potentials of -0.584, -0.606, and -0.622 V vs. RHE. The kinetic parameters listed in Table 2 were varied by ΔX of 5%, while the parameters listed in Table 1 remained constant.

First, it can be observed that the spread of the obtained S_{local} values is significantly smaller. In the analysis shown in Figure 2, the sensitivity fell within a wide range from ≈10^{-9} to ≈10^{2}, whereas in Figure 3, the lower boundary is ≈10^{-3}. It cannot therefore be concluded that the sensitivity of i_{cell} to any of the cathode kinetic parameters is negligible. However, in the model under study, a change in anode kinetics does not affect the total current density. This is due to the adopted computational methodology - a constant cathode potential is assumed, and therefore a change in η_{10} or b of the anode product does not alter i_{cell} on the cathode side.

Since i_{cell} is the same on both the anode and cathode sides, the anode potential has changed. For example, in the base case (51.9 mV/dec), $E_{appl,a}$ was 1.458 V vs. RHE, while with a 5% increase in Tafel slope value (54.5 mV/dec), it was 1.462 V vs. RHE.

The parameter with the greatest influence on i_{cell}, regardless of the potential, is $\eta_{10}^{\mathrm{C_2H_4}}$. This is because C_2H_4 is the main reduction product (Figure 1). The greater the contribution of a given product to i_{cell}, the more sensitive it is to the kinetic parameters of that product. Hence, the S_{local} values for the major products are higher than those for the minor products. Furthermore, for each product, a 5% change in η_{10} has a greater impact than the same change in b.

One of the main contributors to U_{cell}, particularly at high current densities, are ohmic losses caused by the cell's resistance. Therefore, Figure 4 shows a sensitivity analysis with respect to R_{cell}. In the model under consideration, the resistance is independent of the cell current. Thus, the results are presented for a single operating point. As in Figures 2 and 3, the values listed in Table 1 were varied by ΔX of 5%. Parameters that have no effect (S_{local}=0) on the value of R_{cell} have been omitted from the figure.

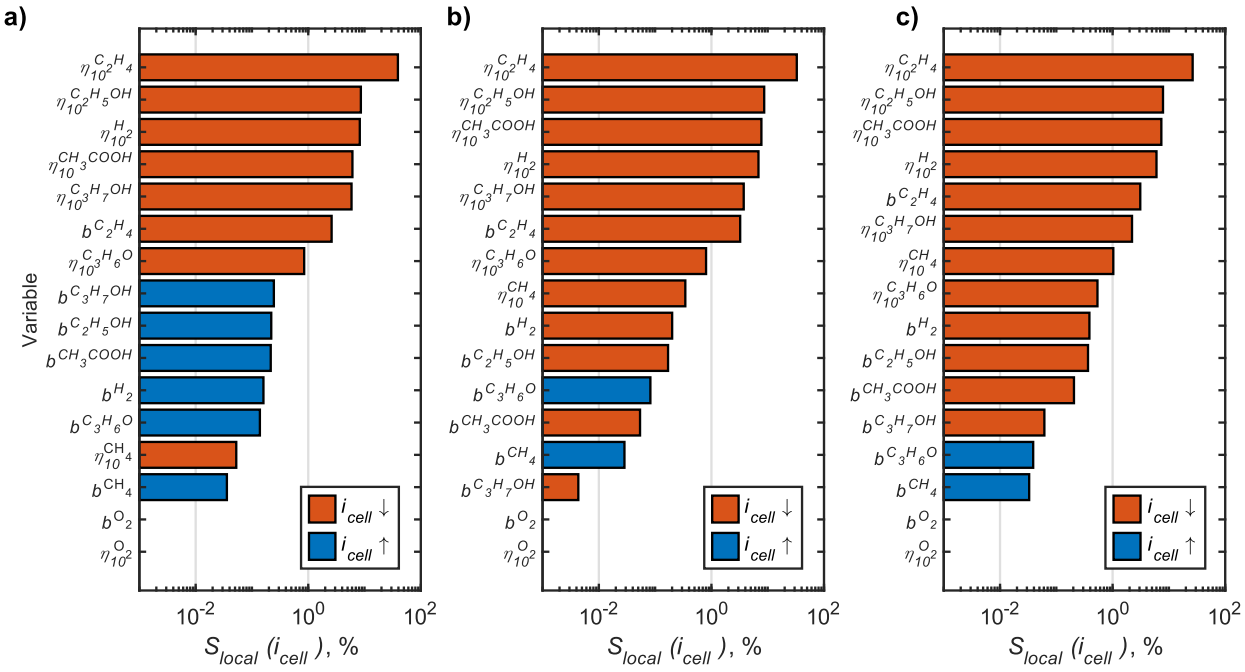

***Figure 3**. Local sensitivity analysis with respect to i_{cell}: values of S_{local} for $\Delta X = 5\%$ at (a) -0.584, (b) -0.606 and (c) -0.622 V vs. RHE for kinetic parameters.*

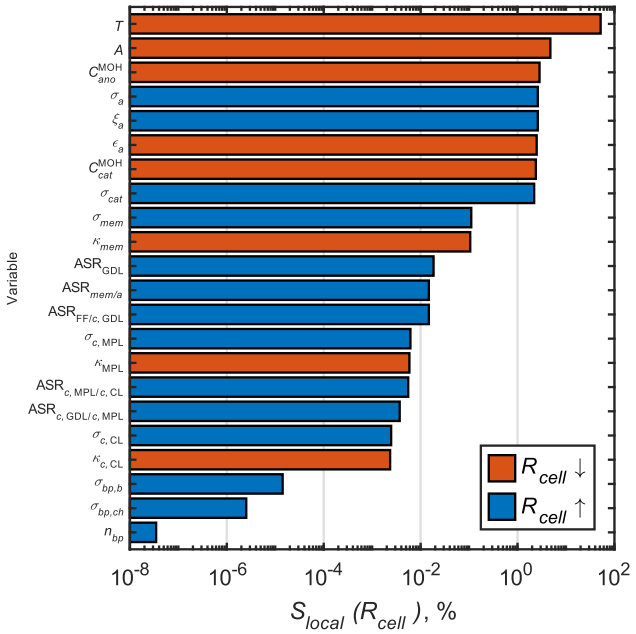

***Figure 4**. Local sensitivity analysis with respect to R_{cell}: values of S_{local} for $\Delta X = 5\%$ for resistance parameters.*

Figure 4 shows that cell resistance is most sensitive to temperature. This is because T affects the conductivity of the cell materials and electrolytes. Second in importance is the cell surface area, since many of the parameters are defined as ASR, and thus the resistance of the components is inversely proportional to A. The subsequent parameters (C_{ano}^{MOH}, σ_a, ξ_a and ϵ_a) relate to the resistance of the anolyte layer, and therefore it has a significant impact on R_{cell}. The same applies to the catholyte, whose parameters have reached similar S_{local} values.

As in Figure 2, a grouping of parameters describing a single cell component can be observed in Figure 4. It can therefore be concluded that the anolyte and catholyte have the greatest influence on resistance, followed by the membrane, interfaces, microporous layer, cathode catalyst layer, and flow-field plate. The parameters of the last component have an impact on R_{cell} that is several orders of magnitude smaller, and the bipolar plate generates minimal ohmic losses.

The values of the S_{local} index presented so far should only be regarded as an indicative view of the model's sensitivity at a specific operating point. As shown, the choice of operating point can significantly alter the sensitivity to individual parameters. Therefore, conclusions regarding the model's overall sensitivity cannot be drawn based on an analysis at a single operating point.

Since the system can operate in a virtually infinite number of states (each described by a unique combination of at least 40 parameters), it is necessary to perform a global sensitivity analysis. Its results are presented in Figures 5 and 6. The analysis was performed for the parameters listed in Table 1, with their values varied within the specified ranges.

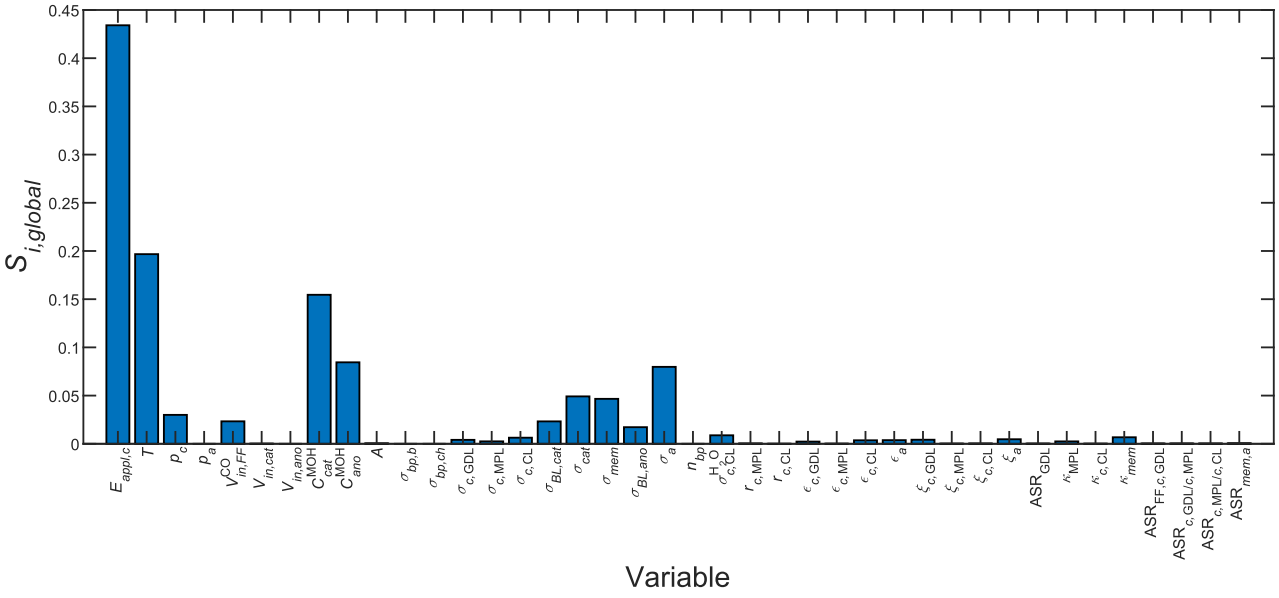

Figure 5. Sobol' first order indices with respect to U_{cell} .

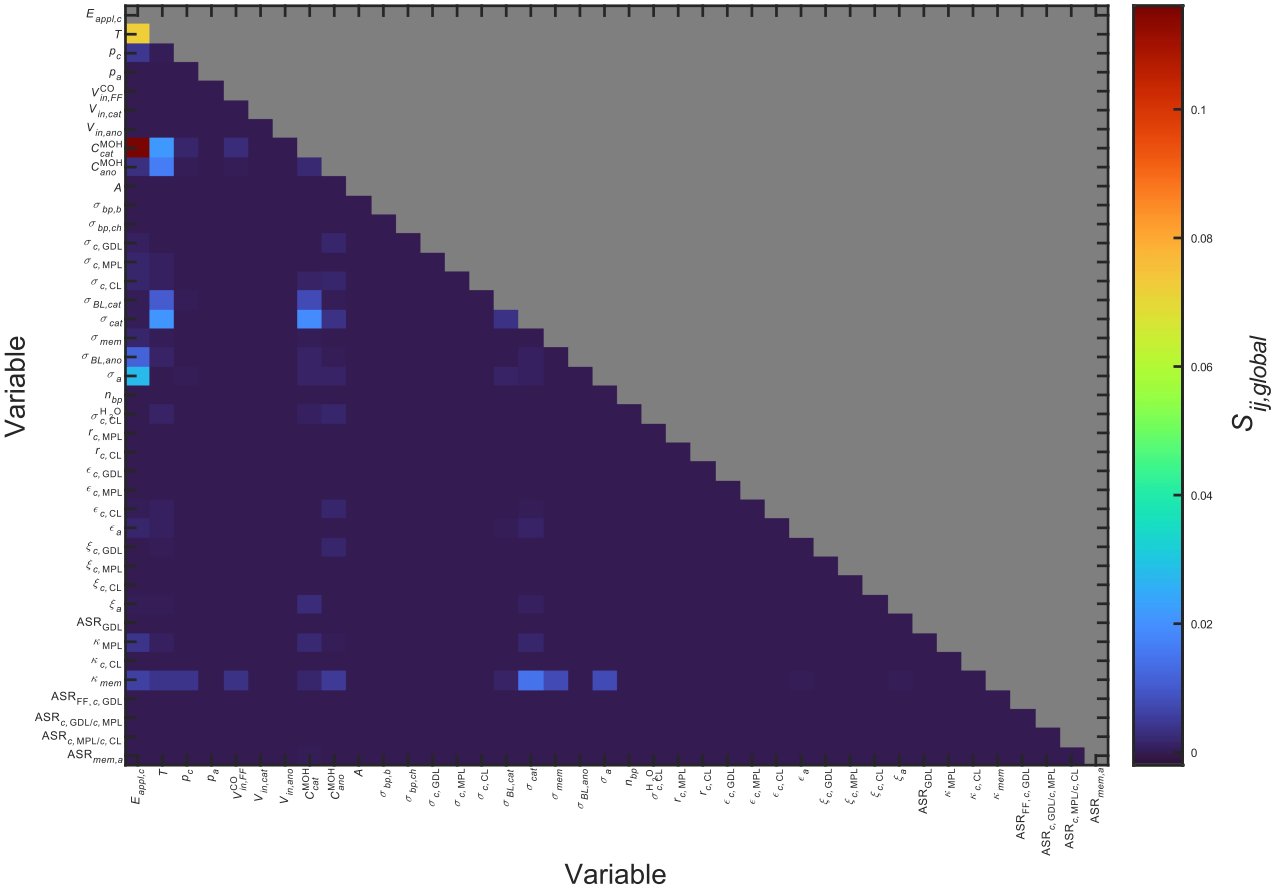

Figure 6. *Sobol' second order indices with respect to* U_{cell}.

Figure 5 shows that U_{cell} is, globally, most sensitive to $E_{appl,c}$ and T, which is consistent with the results of previous local analyses. The following parameters are the electrolyte concentrations. The significant influence of these parameters stems largely from their interaction with other parameters (Figure 6), including temperature and the thickness of the cell layers. In the local analysis, the anode parameters ($\delta_a, \xi_a, \epsilon_a$) were found to have a significant influence. Here, however, only its thickness yielded a high $S_{ij,global}$ value. By contrast, the thicknesses of the cathode, the boundary layers and the membrane were found to have a greater global influence. The other parameters whose influence can be considered significant are p_c and $\dot{V}_{in,\mathrm{FF}}^{\mathrm{CO}}$.

4. Discussion and conclusions

The sensitivity analysis reveals a clear hierarchy of parameters affecting the carbon monoxide electrolysis system. Both local and global analyses identify cathcompeodic applied potential $E_{appl,c}$ and temperature T as the most dominant factors influencing cell voltage U_{cell}.

Despite the high sensitivity, $E_{appl,c}$ is often reported without iR-correction. Without accounting for the ohmic drop, the true kinetics of the catalyst are obscured, making it difficult to compare results across different systems. We therefore recommend that iR-compensated values be treated as a standard requirement for reporting COE performance to ensure data reproducibility and model accuracy.

The same applies to temperature, which is a parameter rarely measured directly within the cell, but at most reported as the ambient temperature at which the experiments were conducted. Beyond its direct local impact, temperature shows some of the highest global interaction indices, meaning its effect is coupled with layer properties and reaction kinetics, among others. For this reason, we believe that the introduction of in-situ temperature measurements would allow for a more informed interpretation of the results.

Another set of parameters for which reporting is usually limited are the dimensions of individual cell elements. This is also a group of parameters that have a relatively significant effect on the cell's voltage. As the dimensions of the components are easily measurable, we recommend reporting their values to improve the data quality.

On the other hand, the parameters that are measured and reported in the vast majority of experimental studies are the volume flow rates of the electrolytes. However, our global and local analyses have shown that these are among the parameters with the least influence on U_{cell}. Therefore, when conducting experimental research, a relatively low accuracy of these measurements is acceptable, and the flow rate should be selected to ensure sufficiently good electrolyte replenishment and removal of products.

This analysis shows that the hierarchy of parameters changes as the operating point changes, and an increase in current density alters the influence of key variables. This justifies the need to perform global sensitivity analyses of electrolysis process models. It should be noted that the results presented refer to the mathematical model described here, and the analysis primarily examined the effect on U_{cell}, which is the main parameter determining efficiency. The sensitivity hierarchy may differ for other research models, systems with different kinetics, and other output variables.

Acknowledgement

The PHOENIX project received funding from the European Union's Horizon Europe research and innovation program under grant agreement No. 101172764. Views and opinions expressed are however those of the author(s) only and do not necessarily reflect those of the European Union or CINEA. Neither the European Union nor the granting authority can be held responsible for them.

References

[1] Nam D-H, Shekhah O, Ozden A, McCallum C, Li F, Wang X, et al. High-Rate and Selective CO2 Electrolysis to Ethylene via Metal–Organic-Framework-Augmented CO2 Availability. Advanced Materials 2022;34:2207088. https://doi.org/10.1002/adma.202207088.

[2] Chen C, Yan X, Liu S, Wu Y, Wan Q, Sun X, et al. Highly Efficient Electroreduction of CO2 to C2+ Alcohols on Heterogeneous Dual Active Sites. Angewandte Chemie International Edition 2020;59:16459–64. https://doi.org/10.1002/anie.202006847.

[3] Rabinowitz J, Kanan M. The future of low-temperature carbon dioxide electrolysis depends on solving one basic problem. Nature Communications 2020;11:5231. https://doi.org/10.1038/s41467-020-19135-8.

[4] Leonard ME, Clarke LE, Forner-Cuenca A, Brown SM, Brushett FR. Investigating Electrode Flooding in a Flowing Electrolyte, Gas-Fed Carbon Dioxide Electrolyzer. ChemSusChem 2020;13:400–11. https://doi.org/10.1002/cssc.201902547.

[5] Fan M, Miao RK, Ou P, Xu Y, Lin Z-Y, Lee T-J, et al. Single-site decorated copper enables energy- and carbon-efficient CO2 methanation in acidic conditions. Nat Commun 2023;14:3314. https://doi.org/10.1038/s41467-023-38935-2.
[6] She X, Zhang T, Li Z, Li H, Xu H, Wu J. Tandem Electrodes for Carbon Dioxide Reduction into C2+ Products at Simultaneously High Production Efficiency and Rate. Cell Reports Physical Science 2020;1:100051. https://doi.org/10.1016/j.xcrp.2020.100051.
[7] Wu G, Song Y, Zheng Q, Long C, Fan T, Yang Z, et al. Selective Electroreduction of CO2 to n-Propanol in Two-Step Tandem Catalytic System. Advanced Energy Materials 2022;12:2202054. https://doi.org/10.1002/aenm.202202054.
[8] Sisler J, Khan S, Ip AH, Schreiber MW, Jaffer SA, Bobicki ER, et al. Ethylene Electrosynthesis: A Comparative Techno-economic Analysis of Alkaline vs Membrane Electrode Assembly vs CO2–CO–C2H4 Tandems. ACS Energy Lett 2021;6:997–1002. https://doi.org/10.1021/acsenergylett.0c02633.
[9] Du H, Fu J, Liu L-X, Ding S, Lyu Z, Chang Y-C, et al. Recent progress in electrochemical reduction of carbon monoxide toward multi-carbon products. Materials Today 2022;59:182–99. https://doi.org/10.1016/j.mattod.2022.08.012.
[10] Ripatti DS, Veltman TR, Kanan MW. Carbon Monoxide Gas Diffusion Electrolysis that Produces Concentrated C2 Products with High Single-Pass Conversion. Joule 2019;3:240–56. https://doi.org/10.1016/j.joule.2018.10.007.
[11] Weng L-C, Bell AT, Weber AZ. Towards membrane-electrode assembly systems for CO2 reduction: a modeling study. Energy Environ Sci 2019;12:1950–68. https://doi.org/10.1039/C9EE00909D.
[12] Weng L-C, Bell AT, Weber AZ. A systematic analysis of Cu-based membrane-electrode assemblies for CO2 reduction through multiphysics simulation. Energy Environ Sci 2020;13:3592–606. https://doi.org/10.1039/D0EE01604G.
[13] Alkayyali T, Zargartalebi M, Ozden A, Arabyarmohammadi F, Dorakhan R, Edwards JP, et al. Pathways to reduce the energy cost of carbon monoxide electroreduction to ethylene. Joule 2024;8:1478–500. https://doi.org/10.1016/j.joule.2024.02.014.
[14] Weng L-C, Bell AT, Weber AZ. Modeling gas-diffusion electrodes for CO_2 reduction. Phys Chem Chem Phys 2018;20:16973–84. https://doi.org/10.1039/C8CP01319E.
[15] Guo S, Liu Y, Huang Y, Wang H, Murphy E, Delafontaine L, et al. Promoting Electrolysis of Carbon Monoxide toward Acetate and 1-Propanol in Flow Electrolyzer. ACS Energy Lett 2023;8:935–42. https://doi.org/10.1021/acsenergylett.2c02502.
[16] Marangio F, Santarelli M, Calì M. Theoretical model and experimental analysis of a high pressure PEM water electrolyser for hydrogen production. International Journal of Hydrogen Energy 2009;34:1143–58. https://doi.org/10.1016/j.ijhydene.2008.11.083.
[17] Chmielniak T, Remiorz L. Entropy analysis of hydrogen production in electrolytic processes. Energy 2020;211:118468. https://doi.org/10.1016/j.energy.2020.118468.
[18] Giglio E, Lanzini A, Santarelli M, Leone P. Synthetic natural gas via integrated high-temperature electrolysis and methanation: Part I—Energy performance. Journal of Energy Storage 2015;1:22–37. https://doi.org/10.1016/j.est.2015.04.002.
[19] Kotowicz J, Hulak D, Remiorz L, Brzęczek M, Böhm Ł, Baszczeńska O, et al. Improving the performance of photoelectrochemical CO reduction through ethylene glycol oxidation. Journal of Power Sources 2026;678:240075. https://doi.org/10.1016/j.jpowsour.2026.240075.
[20] Marr C, Li X. An engineering model of proton exchange membrane fuel cell performance. ARI - An International Journal for Physical and Engineering Sciences 1998;50:190–200. https://doi.org/10.1007/s007770050014.
[21] Landesfeind J, Hattendorff J, Ehrl A, Wall WA, Gasteiger HA. Tortuosity Determination of Battery Electrodes and Separators by Impedance Spectroscopy. J Electrochem Soc 2016;163:A1373. https://doi.org/10.1149/2.1141607jes.
[22] Jouny M, Luc W, Jiao F. High-rate electroreduction of carbon monoxide to multi-carbon products. Nat Catal 2018;1:748–55. https://doi.org/10.1038/s41929-018-0133-2.
[23] Sander R. Compilation of Henry's law constants (version 5.0.0) for water as solvent. Atmospheric Chemistry and Physics 2023;23:10901–2440. https://doi.org/10.5194/acp-23-10901-2023.
[24] Weisenberger S, Schumpe A. Estimation of gas solubilities in salt solutions at temperatures from 273 K to 363 K. AIChE Journal 1996;42:298–300. https://doi.org/10.1002/aic.690420130.
[25] Welty J. Fundamentals of Momentum, Heat and Mass Transfer, 5th Edition. Fundamentals of Momentum, Heat and Mass Transfer, 5th Edition n.d.
[26] Elliott JR, Diky V, Knotts TA, Wilding WV. Properties of Gases and Liquids. 6th Edition. McGraw-Hill Education; 2023.
[27] Pratt KC, Wakeham WA. The mutual diffusion coefficient for binary mixtures of water and the isomers of propanol. Proc R Soc Lond A 1975;342:401–19. https://doi.org/10.1098/rspa.1975.0031.
[28] Sobol′ IM. Global sensitivity indices for nonlinear mathematical models and their Monte Carlo estimates. Mathematics and Computers in Simulation 2001;55:271–80. https://doi.org/10.1016/S0378-4754(00)00270-6.

[29] AvCarb. Gas Diffusion Layers (GDL) - AvCarb Material Solutions 2024. https://www.avcarb.com/products/gas-diffusion-layers-gdl/ (accessed September 24, 2025).
[30] Wang S, Deng X, Wang J, Zhu Y. Experimental measurements of effective electrical conductivities and electrical contact resistances in proton exchange membrane fuel cells. International Journal of Hydrogen Energy 2025;103:556–65. https://doi.org/10.1016/j.ijhydene.2025.01.289.
[31] Jensen JO, Aili D, Hansen MK, Li Q, Bjerrum NJ, Christensen E. A Stability Study of Alkali Doped PBI Membranes for Alkaline Electrolyzer Cells. ECS Trans 2014;64:1175. https://doi.org/10.1149/06403.1175ecst.
[32] Zhou H, Yu F, Sun J, He R, Chen S, Chu C-W, et al. Highly active catalyst derived from a 3D foam of Fe(PO3)2/Ni2P for extremely efficient water oxidation. Proceedings of the National Academy of Sciences 2017;114:5607–11. https://doi.org/10.1073/pnas.1701562114.